Accurate Modeling, Design, and Load Estimation of *LCC*-S Based WPT System With a Wide Range of Load

Shufan Li, Fang Li, Rong Zhang, Chengxuan Tao, *Member, IEEE*, and Lifang Wang, *Member, IEEE*

***Abstract*—Modeling of the wireless power transfer (WPT) system is the premise to design and control it. First harmonic analysis (FHA) is a simple and effective method to model the WPT system, but its accuracy may decrease with the variation of load in a wide range. In this article, harmonics are analyzed in the primary side of an *LCC*-S compensation network based WPT system, depicting a waveform of the output current of the inverter much closer to the real one compared with FHA-based model. In the secondary side, the time-domain analysis is conducted both in continuous conduction mode and discontinuous conduction mode of the rectifier, deriving an equivalent input impedance featuring the nonlinear characteristics of the system. Based on the proposed model, the parameters of the *LCC* network are designed, proving to tune the ZVS condition better than the FHA-based method. Finally, the load of the system is estimated, achieving a high accuracy (with the estimating error less than 5%) in a wide range with a simple sampling method.**

***Index Terms*—Accurate modeling, load estimation, parameter design, wireless power transfer (WPT).**

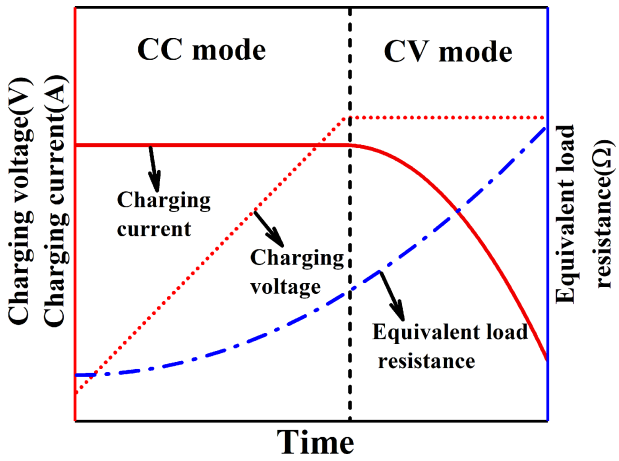

Fig. 1. Charging process of a battery of EVs.

I. Introduction

THE wireless power transfer [1], [2] (WPT) technology are used to transfer power wirelessly through magnetic coupling [3], electric coupling [4], or microwaves [5]. In the past 20 years, this technology has witnessed its great development and wide utilization in electric vehicles [6], unmanned aerial vehicles [7], medical devices [8], portable electronics [9], and other industrial fields.

Manuscript received 28 December 2022; revised 2 March 2023 and 16 April 2023; accepted 17 May 2023. Date of publication 24 May 2023; date of current version 1 September 2023. This work was supported by the National Key R&D Program of China under Grant 2021YFB2501604. Recommended for publication by Associate Editor M. Liu. *(Corresponding author: Shufan Li.)*

Shufan Li, Fang Li, Rong Zhang, and Lifang Wang are with the Key Laboratory of Power Electronics and Electric Drives, Institute of Electrical Engineering, Chinese Academy of Sciences, Beijing 100190, China, and also with the University of Chinese Academy of Sciences, Beijing 100190, China (e-mail: lishufan@mail.iee.ac.cn; lifang@mail.iee.ac.cn; zhangrong@mail.iee.ac.cn; wlf@mail.iee.ac.cn).

Chengxuan Tao is with the Key Laboratory of Power Electronics and Electric Drives, Institute of Electrical Engineering, Chinese Academy of Sciences, Beijing 100190, China, also with the University of Chinese Academy of Sciences, Beijing 100190, China, and also with the School of Mechanical Engineering, Beijing Institute of Technology, Beijing 100081, China (e-mail: taochengxuan@mail.iee.ac.cn).

Color versions of one or more figures in this article are available at https://doi.org/10.1109/TPEL.2023.3279659.

Digital Object Identifier 10.1109/TPEL.2023.3279659

Recently, the focus of WPT is mainly on the improvement of power transfer efficiency [10], misalignment of the coupling coils [11], bidirectional/dynamic WPT [12], [13], topologies and controlling of the system [14], [15], foreigner object detection [16], and so on. For all the above topics, there is a common premise—the modeling of the system, which has been studied since the emerging of WPT technology. Coupled-mode [17], *S*-parameters [18], equivalent circuit [19], and other theories have been taken to model the WPT system, while the models built based on different theories imply the same essence and can be conversed and deduced by each other. Among the theories mentioned above, equivalent circuit model depicts the WPT system more clearly and can reflect the relations of parameters, thus is favored by many researchers [20], [21], [22]. To simplify the modeling and calculation, first harmonic analysis (FHAs) are often used to model the equivalent circuit. For example, the equivalent input impedance of the rectifier in the secondary side are usually considered as a resistive impedance [23], which has been proved inaccurate especially in the discontinuous conduction mode (DCM) of the rectifier [24].

DCM usually occurs when the load of the WPT system deviates a lot from the nominal load [25]. A typical scenario is the charging of battery for the EVs. As shown in Fig. 1, the charging process of a battery of EVs usually contains constant current and constant voltage (CV) stage [26], [27]. The equivalent load of

the WPT system will increase with the voltage of battery [28]. In CV stage, the value of the equivalent load will be so large that DCM of the rectifier may occur.

To model the WPT system more accurately, numerical solutions of DCM are given in [25], which is simple but lacks universality. Time-domain analysis (TDA) are taken in [29] and [30], where nonlinear characteristics of the system caused by semiconductor MOSFETs or diodes are considered, and the TDA are proved to depict both fundamental and harmonics of the waveforms and thereby improve the modeling accuracy. In [24], both the primary and secondary side of an SS network based WPT system are modeled with TDA, which are proved superior to FHA. However, the TDA method will be very complicated to apply to both sides of the WPT system, especially when there is a high-order compensation network.

Accurate modeling makes it possible to estimate the load of the system, which can help to monitor and control the power transfer in the primary side without the use of communication. According to [31], the parameter estimation method is divided into four categories including nonzero receiver reactance method, energy injection method, reconfigurable circuit method, and frequency sweeping method. With such methods, the high-frequency voltage, current, or frequency itself are usually sampled to calculate mutual inductance, load, or other parameters of the system. No matter which method is taken, two points are usually focused: sampling rate and estimation accuracy. Most load estimating methods takes high sampling rate to sample the high-frequency voltage or current in the primary side, which occupies many computing resources of the controller and may lower the controlling speed. The energy injection method is an exception since it only samples the envelope of the transmitter current [32]. However, the method is offline and is not applicable to an operating system. There are also methods sampling the dc input current of the system to simplify the sampling [33], the accuracy of which is good in a specific range maintaining continuous conduction mode (CCM) of the rectifier, but doubtful in DCM. The problem, in fact, involves the second focus mentioned above, the load estimation accuracy in a wide range. The load of the WPT system can change in a wide range (CV charging for a battery, for example), the results of estimation may drift in DCM if the estimation method is based on a CCM model. DCM mode of the rectifier is considered in [34], of which the load estimating error for DCM can be less than 2%, but the error will increase when the load is in a critical state of CCM and DCM.

In this article, the *LCC*-S based WPT system is modeled accurately both in primary and secondary side. In the primary side, harmonics of the output voltage and current of the inverter are taken into consideration which highly improves the accuracy of the modeling; in the secondary side, the input voltage and current are modeled with TDA, thus deriving an equivalent input impedance of the rectifier in the CCM and DCM, respectively. Based on the above model, the parameters of the *LCC* compensation network are designed. Besides, a load estimation method based on the accurate model is proposed. Compared with the previous article, the contribution of the article is to improve the modeling accuracy of the WPT system with a wide range of load, and meantime to improve the accuracy of load estimation with a much easier sampling method.

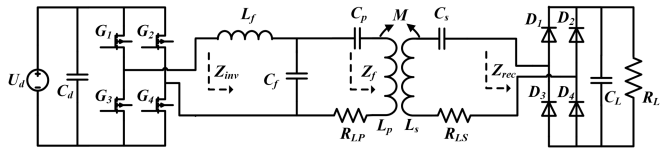

Fig. 2. Typical WPT system.

II. WPT System Based on *LCC*-S Compensation Network

A WPT system is as Fig. 2 shows. L_P and L_S are self-inductance of primary and secondary coil, respectively, among which the mutual inductance is M, R_{LP} and R_{LS} are their parasitic resistance. The full-bridge inverter contains four MOSFETs G_1–G_4, the output power of which will be tuned by the compensation network L_f–C_f–C_p. The impedance of the three arms of the compensation network should be equal, thus the values of L_f, C_f, and C_p are

$$\begin{cases} L_f = & X_p/\omega \\ C_f = & 1/X_p/\omega \\ C_p = & 1/\omega/(\omega L_p - \alpha X_p) \end{cases} \tag{1}$$

where X_p is the impedance of the three arms, and α is used to realize the ZVS condition of the inverter, which will be discussed later. The angular frequency $\omega = 2\pi f$, while f is the switching frequency of the inverter.

The amplitude of current in the primary side coil is

$$I_p = \frac{4}{\pi X_p} U_d. \tag{2}$$

The capacitor C_s is used to form a resonant network with L_s, and it can be determined by

$$C_s = 1/\omega^2/L_s. \tag{3}$$

The rectifier contains four diodes D_1–D_4, and a capacitor C_L works as a voltage filter followed by the load R_L. If the harmonics are neglected, the input impedance of the rectifier can be derived as

$$R_e = \frac{8}{\pi^2} R_L. \tag{4}$$

The amplitude of the induced voltage in the secondary side coil is

$$U_s = \omega M I_p. \tag{5}$$

The output power can be derived as

$$P_o = \frac{\omega^2 M^2 U_d^2}{X_p^2 R_L}. \tag{6}$$

The power transfer efficiency is

$$\eta = \frac{P_o}{P_o + \frac{1}{2} I_p^2 R_{LP} + \frac{1}{2} I_s^2 R_{LS}} \tag{7}$$

where I_s is the amplitude of current in the secondary side coil.

III. Accurate Modeling of the WPT System in the Primary Side

FHA method is an easy way to analyze the WPT system, but it will lead to errors in conditions when accuracy is needed, for example, in parameter estimation and controlling of the system. Harmonics are taken into consideration in this article to model the WPT system, improving the accuracy of modeling.

The output voltage waveform of the inverter is a square wave, and it can be described by

$$u_{\mathrm{inv\_n}}(t) = \frac{4U_d}{n\pi}\sin(n\omega t), \quad n = 1, 3, 5 \ldots . \tag{8}$$

The phasor form of (8) is

$$U_{\mathrm{inv\_n}} = \frac{4U_d}{n\pi} \angle -90^\circ, \quad n = 1, 3, 5 \ldots . \tag{9}$$

The fundamental output impedance of the inverter is

$$Z_{\mathrm{inv\_1}} = jX_p + \frac{(-jX_p).(j\alpha X_p + Z_f)}{j(\alpha-1)X_p + Z_f} = \frac{X_p^2}{j(\alpha-1)X_p + Z_f} \tag{10}$$

where Z_f is the reflected impedance.

The fundamental component of the output current of inverter can be calculated as

$$\boldsymbol{I}_{\mathrm{inv\_1}} = \frac{4U_d}{\pi X_p^2}\sqrt{R_f^2 + X_{f\_p}^2} \angle \left(-90^\circ + \arctan\frac{X_{f\_p}}{R_f}\right) \tag{11}$$

where

$$X_{f\_p} = X_f + (\alpha - 1)X_p \tag{12}$$

and R_f and X_f are the real and imaginary part of Z_f, respectively.

Thus, the time domain form of $\boldsymbol{I}_{\mathbf{inv\_1}}$ is

$$i_{\mathrm{inv\_1}}(t) = \frac{4U_d}{\pi X_p^2}\left[R_f \sin(\omega t) + X_{f\_p}\cos(\omega t)\right]. \tag{13}$$

As for the harmonic component, only the L_f–C_f loop is considered because of the filtering characteristics of the *LCC* network [35]. When L_f and C_f resonate at the operating frequency f, the L_f–C_f loop is a low-pass filter to the high-frequency harmonics, and

$$Z_{\mathrm{inv\_n}} \approx jn\omega L_f + \frac{1}{jn\omega C_f} = j\frac{n^2-1}{n}X_p, \quad n = 3, 5, 7 \ldots . \tag{14}$$

The harmonic component of $\boldsymbol{I}_{\mathrm{inv}}$ is

$$\boldsymbol{I}_{\mathrm{inv\_n}} \approx \frac{4U_d}{(n^2-1)\pi X_p} \angle -180^\circ, \quad n = 3, 5, 7 \ldots . \tag{15}$$

The time-domain form of $\boldsymbol{I}_{\mathbf{inv\_}n}$ is

$$i_{\mathrm{inv\_n}}(t) \approx -\frac{4U_d}{(n^2-1)\pi X_p}\cos(n\omega t), \quad n = 3, 5, 7 \ldots . \tag{16}$$

According to (13) and (16), the output current of inverter can be derived as

$$i_{\mathrm{inv}}(t) = \frac{4U_d}{\pi X_p^2}\left[R_f \sin(\omega t) + X_{f\_p}\cos(\omega t)\right] - \sum_{n=3,5,7}^{\infty}\frac{4U_d}{(n^2-1)\pi X_p}\cos(n\omega t). \tag{17}$$

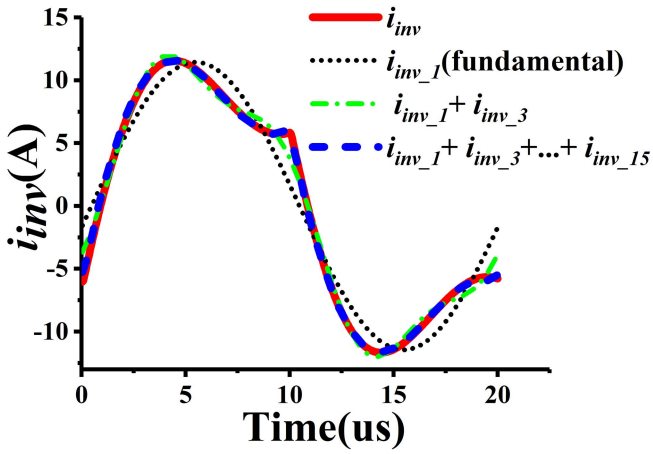

Fig. 3. Waveforms of i_{inv}.

Fig. 3 shows the waveforms of i_{inv}, it can be seen that (17) can feature the simulated output current of inverter closely.

In the above analysis, the parasitic resistance of L_f, C_f, C_p, and L_p are neglected. This simplification can be explained from the view of power losses. According to (2), the amplitude of the voltage on R_{Lp} can be derived by

$$U_{\mathrm{RLP}} = \frac{4U_d R_{LP}}{\pi X_p}. \tag{18}$$

To improve the power transfer efficiency, the power losses in the primary coil should be very small, therefore the value of U_{RLP} should be very small. Considering that U_d can be hundreds of volts, the ratio of R_{LP} and X_p should be far less than 1, which means $R_{LP} << X_p$. The parasitic resistance of L_f, C_f, and C_p are usually less than R_{LP}. To conclude, the parasitic resistance of the primary-side coil and compensation network are extremely small compared with the inductive or capacitive resistance with which they are in series, thus they can be neglected.

IV. Accurate Modeling of the WPT System in the Secondary Side

Based on the state of the four diodes of the rectifier, the operating modes of the secondary side of the WPT system can be divided into three states (states 1, 2, and 3 shown in Fig. 4), which will be analyzed in detail below.

A. Continuous Conduction Mode (CCM)

Fig. 5 shows the waveforms of the secondary side, where u_s is the induced voltage of the secondary side, i_L is the current in L_s and C_s, u_C is the voltage of C_s, and u_r is the input voltage of the rectifier. To analyze the waveforms, we first assume a phase angle of u_s, i.e.,

$$u_{s\_a} = U_s \sin(\omega t + \theta). \tag{19}$$

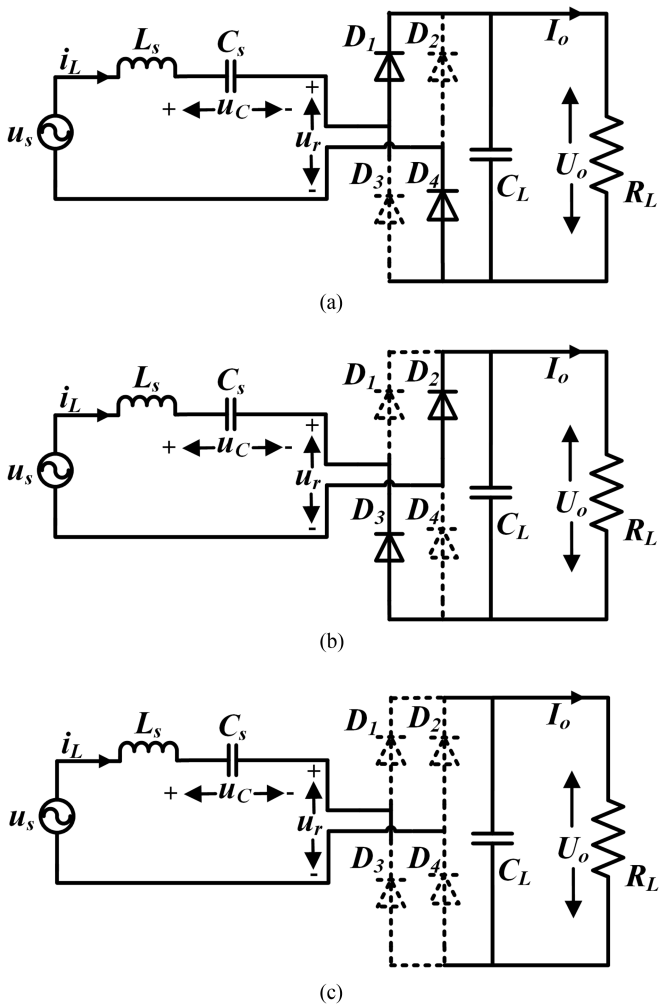

Fig. 4. Operating modes of the secondary side of the WPT system. (a) State 1. (b) State 2. (c) State 3.

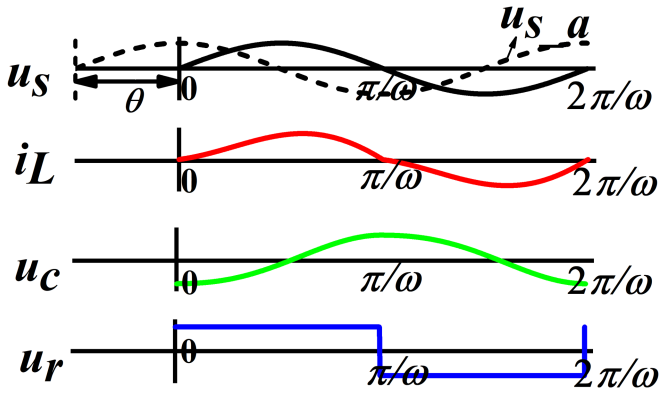

Fig. 5. Waveforms of the secondary side (CCM).

Next, the full cycle of the waveforms in Fig. 5 will be analyzed in two parts separated by π/ω.

1) $0 < t \leq \pi/\omega$*:* During this half of the cycle, the waveforms correspond to state 1 of Fig. 4. The state-space equation of the system can be derived as

$$\dot{\boldsymbol{x}}(t) = \boldsymbol{A}\boldsymbol{x}(t) + \boldsymbol{B}\boldsymbol{u}(t) \tag{20a}$$

where

$$\dot{\boldsymbol{x}}(t) = \begin{bmatrix} i_L(t) \\ u_C(t) \end{bmatrix}, \ \boldsymbol{A} = \begin{bmatrix} 0 & -\frac{1}{L_s} \\ \frac{1}{C_s} & 0 \end{bmatrix}, \ \boldsymbol{B} = \begin{bmatrix} \frac{1}{L_s} & m\frac{1}{L_s} \\ 0 & 0 \end{bmatrix},$$
$$\boldsymbol{u}(t) = \begin{bmatrix} U_s \sin(\omega t + \theta) \\ U_o \end{bmatrix}, \quad U_o = U_{\mathrm{RL}} + 2V_{d\_f} \tag{20b}$$

where U_{RL} is voltage of the load, V_{d_f} is the forward voltage of the diodes, and m $= -1$.

Equation (20) can be solved by

$$\boldsymbol{x}(t) = \boldsymbol{\Phi}(t)\boldsymbol{x}(0) + \int_0^t \boldsymbol{\Phi}(t-\tau)\boldsymbol{B}\boldsymbol{u}(\tau)d\tau$$
$$= \begin{bmatrix} \frac{U_s}{2\omega L_s}[\omega t \sin(\omega t + \theta) + \sin\omega t \sin\theta - 2G\sin\omega t \\ -2G_{c0}\sin\omega t] \\ \frac{U_s}{2}[-\omega t\cos(\omega t + \theta) + \sin\omega t\cos\theta + 2G(\cos\omega t - 1) \\ +2G_{c0}\cos\omega t] \end{bmatrix} \tag{21}$$

where

$$\boldsymbol{\Phi}(t) = \begin{bmatrix} \cos(\omega t) & -\frac{1}{\omega L_s}\sin(\omega t) \\ \omega L_s \sin(\omega t) & \cos(\omega t) \end{bmatrix}, \ \boldsymbol{x}(0) = \begin{bmatrix} 0 \\ u_C(0) \end{bmatrix} \tag{22}$$

and G and G_{c0} are the ratio of U_o and U_{c0} to U_s, separately.

According to antisymmetry property [19]

$$\boldsymbol{x}\left(\frac{\pi}{\omega}\right) = -\boldsymbol{x}(0). \tag{23}$$

By solving (23), it can be derived that

$$\begin{cases} \theta = 0 \\ \mathrm{G} = \frac{U_o}{U_s} = \frac{\pi}{4}. \end{cases} \tag{24}$$

The output voltage gain G is a constant, meaning that *LCC*-S compensation network features a characteristic of CV under CCM state of the rectifier.

By substituting (24) into (21), the input current of the rectifier can be written as

$$i_L(t) = \frac{U_s \sin(\omega t)}{\omega L_s}\left(\frac{1}{2}\omega t - \frac{\pi}{4} - G_{c0}\right). \tag{25}$$

Thus, the current of the load is

$$I_o = \frac{\omega}{\pi}\int_0^{\frac{\pi}{\omega}} i_L(t)dt = \frac{U_o}{R_L}. \tag{26}$$

According to (25) and (26), G_{c0} can be calculated as

$$G_{c0} = -\frac{\pi^2 \omega L_s}{8R_L}. \tag{27}$$

Accordingly, the state variables are

$$\boldsymbol{x}(t) = \begin{bmatrix} \frac{U_s \sin(\omega t)}{\omega L_s}\left(\frac{1}{2}\omega t - \frac{\pi}{4} + \frac{\pi^2 \omega L_s}{8R_L}\right) \\ U_s\left[\frac{1}{2}\sin(\omega t) + (-\frac{1}{2}\omega t + \frac{\pi}{4} - \frac{\pi^2 \omega L_s}{8R_L})\cos(\omega t) - \frac{\pi}{4}\right] \end{bmatrix}. \tag{28}$$

2) $\pi/\omega < t < 2\pi/\omega$: During this half of the cycle, the waveforms correspond to state 2 of Fig. 4. The state-space equation of the system can also be written as (20), same as state 1 except that $m = 1$. The deduction of the state equation is similar with the first half of the cycle, and we would not elaborate it here to save space of the article.

During the full cycle, i_L(t) can be derived as

$$i_L(t) = \begin{cases} \frac{U_s \sin(\omega t)}{\omega L_s}\left(\frac{1}{2}\omega t - \frac{\pi}{4} + \frac{\pi^2 \omega L_s}{8R_L}\right) & t \in [0, \frac{\pi}{\omega}] \\ \frac{U_s \sin(\omega t)}{\omega L_s}\left(\frac{1}{2}\omega t - \frac{3\pi}{4} + \frac{\pi^2 \omega L_s}{8R_L}\right) & t \in (\frac{\pi}{\omega}, \frac{2\pi}{\omega}]. \end{cases} \tag{29}$$

As a square wave, $u_r(t)$ can be written as

$$u_r(t) = \begin{cases} U_o & t \in [0, \frac{\pi}{\omega}] \\ -U_o & t \in (\frac{\pi}{\omega}, \frac{2\pi}{\omega}]. \end{cases} \tag{30}$$

The fundamental components of i_L and u_r can be written as

$$\begin{cases} i_{L\_1st} = a_i \cos\omega t + b_i \sin\omega t \\ u_{r\_1st} = a_u \cos\omega t + b_u \sin\omega t \end{cases} \tag{31}$$

where a_i, b_i, a_u, and b_u can be derived with

$$\begin{cases} a_i = \frac{\omega}{\pi}\int_0^{2\pi/\omega} i_L(t)\cos(\omega t)dt = -\frac{U_s}{4\omega L_s} \\ b_i = \frac{\omega}{\pi}\int_0^{2\pi/\omega} i_L(t)\sin(\omega t)dt = \frac{\pi^2 U_s}{8R_L} \\ a_u = \frac{\omega}{\pi}\int_0^{2\pi/\omega} u_r(t)\cos(\omega t)dt = 0 \\ b_u = \frac{\omega}{\pi}\int_0^{2\pi/\omega} u_r(t)\sin(\omega t)dt = U_s. \end{cases} \tag{32}$$

Considering that $a_i < 0$, the real and imaginary part of the equivalent input impedance of the rectifier can be derived as

$$\begin{cases} R_{\text{rec}} = \sqrt{\frac{a_u^2+b_u^2}{a_i^2+b_i^2}}\cos[\arctan\frac{b_u}{a_u} - (\pi - \arctan\frac{b_i}{a_i})] \\ = 8\pi^2 R_L/(\pi^4 + 4\beta^2) \\ X_{\text{rec}} = \sqrt{\frac{a_u^2+b_u^2}{a_i^2+b_i^2}}\sin[\arctan\frac{b_u}{a_u} - (\pi - \arctan\frac{b_i}{a_i})] \\ = 16\beta R_L/(\pi^4 + 4\beta^2) \end{cases} \tag{33}$$

where

$$\beta = R_L/\omega L_s. \tag{34}$$

The both sides of equations in (33) can be divided by ωL_s, i.e.,

$$\begin{cases} R_{\text{rec}\_\beta} = 8\pi^2\beta/(\pi^4 + 4\beta^2) \\ X_{\text{rec}\_\beta} = 16\beta^2/(\pi^4 + 4\beta^2) \end{cases} \tag{35}$$

where R_{rec_β} and X_{rec_β} are the ratio of R_{rec} and X_{rec} to ωL_s, separately.

B. Discontinuous Conduction Mode (DCM)

When the value of load is large enough, the rectifier will enter DCM, the reason of which is elaborated in the Appendix.

Fig. 6 shows the waveforms of u_s, i_L, u_C, and u_r in the DCM mode of the rectifier, the discontinuous angle of i_L is φ.

Depending on the state of i_L, the operating modes of the system can be divided into four states:

1) $0 < t \le \varphi/\omega$: During this state, the waveforms correspond to state 3 of Fig. 4, and u_c remains constant because there is no current flowing through C_s, thus

$$\boldsymbol{x}(t) = \begin{bmatrix} 0 \\ u_c(0) \end{bmatrix}. \tag{36}$$

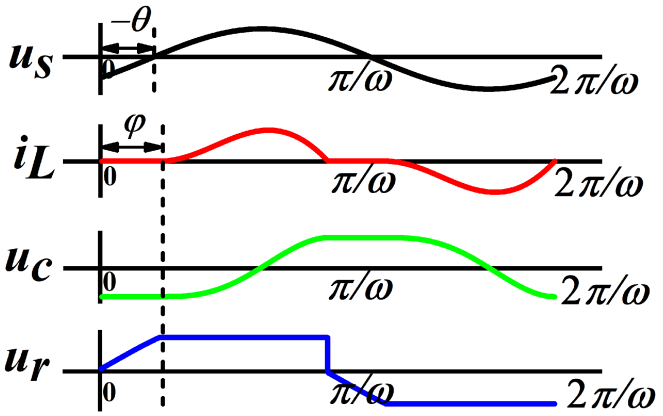

Fig. 6. Waveforms of the secondary side (DCM).

When $t = \varphi/\omega$,

$$u_r\left(\frac{\varphi}{\omega}\right) = U_o = U_s\sin(\varphi + \theta) - u_c(0). \tag{37}$$

2) $\varphi/\omega < t \le \pi/\omega$: During this state, the waveforms correspond to state 1 of Fig. 4, and the state-space equation is

$$\dot{\boldsymbol{x}}(t) = \boldsymbol{A}\boldsymbol{x}(t) + \boldsymbol{B}\boldsymbol{u}(t) \tag{38a}$$

where

$$\dot{\boldsymbol{x}}(t) = \begin{bmatrix} i_L(t) \\ u_C(t) \end{bmatrix}, \boldsymbol{A} = \begin{bmatrix} 0 & -\frac{1}{L_s} \\ \frac{1}{C_s} & 0 \end{bmatrix}, \boldsymbol{B} = \begin{bmatrix} \frac{1}{L_s} & m\frac{1}{L_s} \\ 0 & 0 \end{bmatrix},$$
$$\boldsymbol{u}(t) = \begin{bmatrix} U_s\sin(\omega t + \theta) \\ U_o \end{bmatrix}, \quad U_o = U_{\text{RL}} + 2V_{d\_f}. \tag{38b}$$

Equation (38) can be solved by

$$\boldsymbol{x}(t) = \boldsymbol{\Phi}(t)\boldsymbol{x}(\tfrac{\varphi}{\omega}) + \int_{\frac{\varphi}{\omega}}^{t}\boldsymbol{\Phi}(t-\tau)\boldsymbol{B}\boldsymbol{u}(\tau)d\tau$$
$$= \begin{bmatrix} \frac{U_s}{2\omega L_s}[(\omega t - \varphi)\sin(\omega t + \theta) - \sin(\varphi + \theta)\sin(\omega t - \varphi)] \\ U_s[\frac{3}{4}\sin(\omega t + \theta) - \frac{1}{4}\sin(\omega t - \theta - 2\varphi) \\ -\frac{1}{2}(\omega t - \varphi)\cos(\omega t + \theta) - G] \end{bmatrix}. \tag{39}$$

According to antisymmetry property, (23) also suits for DCM, thus it can be derived that

$$\begin{cases} \cos(2\varphi + \theta) + 2(\varphi\pi)\sin\theta - \cos\theta = 0 \\ 2(\pi\varphi)\cos\theta - 3\sin\theta - \sin(2\varphi + \theta) + 4\sin(\varphi + \theta) = 8G. \end{cases} \tag{40}$$

3) $\pi/\omega < t \le (\pi+\varphi)/\omega$: During this state, the waveforms correspond to state 3 of Fig. 4, and u_c remains constant because there is no current flowing through C_s, thus

$$\boldsymbol{x}(t) = \begin{bmatrix} 0 \\ -u_c(0) \end{bmatrix}. \tag{41}$$

4) $(\pi + \varphi)/\omega < t \le 2\pi/\omega$: During this state, the waveforms correspond to state 1 of Fig. 4. The state-space equation of the system can also be written as (30), same as state 1 except that $m = 1$. The deduction of the state equation is similar with state 2.

During the full cycle, $i_L(t)$ can be derived as

$i_L(t) =$

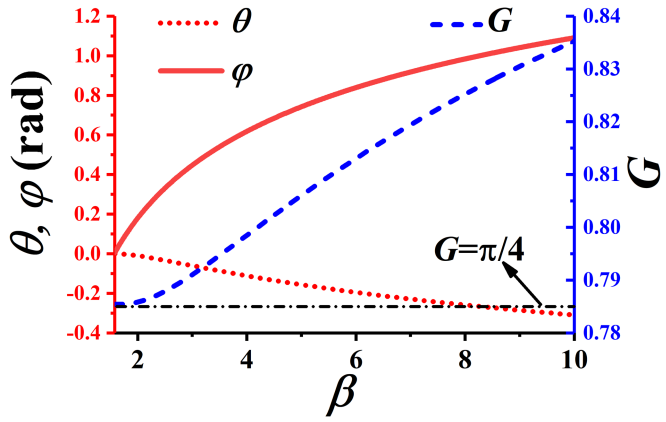

Fig. 7. Relation of φ, θ, and G with β.

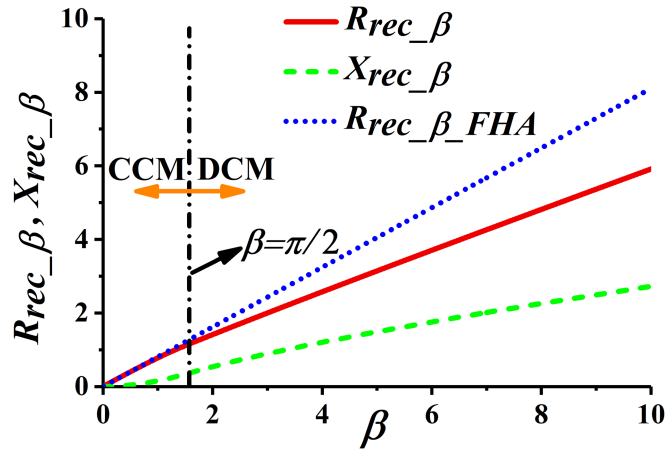

Fig. 8. Relation of $R_{\mathrm{rec\_}\beta}$ and $X_{\mathrm{rec\_}\beta}$ with β.

$$\begin{cases} 0 & t\in[0,\frac{\varphi}{\omega}] \\ \frac{U_s}{2\omega L_s}[(\omega t-\varphi)\sin(\omega t+\theta) & \\ -\sin(\varphi+\theta)\sin(\omega t-\varphi)] & t\in(\frac{\varphi}{\omega},\frac{\pi}{\omega}] \\ 0 & t\in(\frac{\pi}{\omega},\frac{\varphi+\pi}{\omega}] \\ \frac{U_s}{2\omega L_s}[(\omega t-\varphi-\pi)\sin(\omega t+\theta) & \\ -\sin(\varphi+\theta)\sin(\omega t-\varphi)] & t\in(\frac{\varphi+\pi}{\omega},\frac{2\pi}{\omega}]. \end{cases} \tag{42}$$

According to (26) and (42), it can be deduced that

$$\beta\left[2(\pi-\varphi)\cos\theta-3\sin\theta-\sin(2\varphi+\theta)-4\sin(\varphi+\theta)\right]=4\pi G. \tag{43}$$

By combining (40) and (43), it can be found that the values of φ, θ, and G are only related to β. The three equations in (40) and (43) can be solved with mathematical calculation tools (MATLAB, for example), and before the calculation, the range of variables should be defined as $-\pi \le \theta \le \pi$; $0 \le \varphi \le \pi$; $G > 0$. The results of calculation are shown in Fig. 7. θ decreases from 0 with the increase of β, while φ increases from 0 with the increase of β. G increases from $\pi/4$ with the increase of β, signifying that the output voltage will be larger than the nominal voltage if there is no any controlling.

Assuming $\varphi = 0$, the critical condition of CCM and DCM can be derived as

$$\begin{cases} \theta = 0 \\ \beta = \frac{\pi}{2}. \end{cases} \tag{44}$$

$u_r(t)$ can be easily calculated by combining Fig. 6 and (37)

$$u_r(t)=\begin{cases} U_s[\sin(\omega t+\theta)-\sin(\varphi+\theta)+G & t\in[0,\frac{\varphi}{\omega}] \\ GU_s & t\in(\frac{\varphi}{\omega},\frac{\pi}{\omega}] \\ U_s[\sin(\omega t+\theta)+\sin(\varphi+\theta)-G] & t\in(\frac{\pi}{\omega},\frac{\pi+\varphi}{\omega}] \\ -GU_s & t\in(\frac{\pi+\varphi}{\omega},\frac{2\pi}{\omega}]. \end{cases} \tag{45}$$

The fundamental components of i_L and u_r can also be written as (31), the same as CCM, but the values of a_i, b_i, a_u, and b_u are different, which can be derived as

$$\begin{cases} a_i=\frac{\omega}{\pi}\int_0^{2\pi/\omega} i_L(t)\cos(\omega t)dt & =\frac{U_s}{8\pi\omega L_s}F_1(\varphi,\theta) \\ b_i=\frac{\omega}{\pi}\int_0^{2\pi/\omega} i_L(t)\sin(\omega t)dt & =\frac{U_s}{4\pi\omega L_s}F_2(\varphi,\theta) \\ a_u=\frac{\omega}{\pi}\int_0^{2\pi/\omega} u_r(t)\cos(\omega t)dt & =U_s\sin\theta \\ b_u=\frac{\omega}{\pi}\int_0^{2\pi/\omega} u_r(t)\sin(\omega t)dt & =U_s\cos\theta \end{cases} \tag{46}$$

where

$$\begin{cases} F_1(\varphi,\theta)=(1+2\pi^2+2\varphi^2-4\pi\varphi)\sin\theta+2(\varphi-\pi) \\ \quad\times\cos(2\varphi+\theta)-\sin(2\varphi+\theta) \\ F_2(\varphi,\theta)=(\pi^2+\varphi^2-2\pi\varphi-1)\cos\theta+\cos(2\varphi+\theta)+(\varphi-\pi) \\ \quad\times\sin(2\varphi+\theta)+(\varphi-\pi)\sin\theta. \end{cases} \tag{47}$$

Considering that a_i, $a_u < 0$ (which will be discussed in the Appendix), the equivalent input impedance of the rectifier is

$$\begin{cases} R_{\mathrm{rec}}=\sqrt{\frac{a_u^2+b_u^2}{a_i^2+b_i^2}}\cos[(\pi-\operatorname{acr\,tan}\frac{b_u}{a_u})-(\pi-\operatorname{acr\,tan}\frac{b_i}{a_i})] \\ X_{\mathrm{rec}}=\sqrt{\frac{a_u^2+b_u^2}{a_i^2+b_i^2}}\sin[(\pi-\operatorname{acr\,tan}\frac{b_u}{a_u})-(\pi-\operatorname{acr\,tan}\frac{b_i}{a_i})]. \end{cases} \tag{48}$$

Accordingly, $R_{\mathrm{rec\_}\beta}$ and $X_{\mathrm{rec\_}\beta}$ can be derived as

$$\begin{cases} R_{\mathrm{rec\_}\beta}=\frac{8\pi[\sin\theta F_1(\varphi,\theta)+2\cos\theta F_2(\varphi,\theta)]}{\sqrt{F_1(\varphi,\theta)^2+4F_2(\varphi,\theta)^2}} \\ X_{\mathrm{rec\_}\beta}=\frac{8\pi[-\cos\theta F_1(\varphi,\theta)+2\sin\theta F_2(\varphi,\theta)]}{\sqrt{F_1(\varphi,\theta)^2+4F_2(\varphi,\theta)^2}}. \end{cases} \tag{49}$$

It can be concluded from (49) that $R_{\mathrm{rec\_}\beta}$ and $X_{\mathrm{rec\_}\beta}$ are only related to φ and θ, which means they are only related to β. Fig. 8 shows the relation of $R_{\mathrm{rec\_}\beta}$ and $X_{\mathrm{rec\_}\beta}$ with β. The equivalent resistance of the rectifier based on FHA method is also shown in Fig. 8, where $R_{\mathrm{rec\_}\beta\_\mathrm{FHA}} = 8\beta/\pi^2$. In CCM of the rectifier, $R_{\mathrm{rec\_}\beta}$ is close to $R_{\mathrm{rec\_}\beta\_\mathrm{FHA}}$, and the value of $X_{\mathrm{rec\_}\beta}$ is small, it is reasonable to use FHA to model the system approximately. However, in DCM of the rectifier, the gap between $R_{\mathrm{rec\_}\beta}$ and $R_{\mathrm{rec\_}\beta\_\mathrm{FHA}}$ increases with β, and $X_{\mathrm{rec\_}\beta}$ also rises with β and cannot be neglected. Therefore, it is necessary to model the system with TD method in DCM of the rectifier.

In the above analysis, the parasitic resistance of L_s, C_s, and the diodes in the rectifier are neglected. This simplification can be explained from the view of power losses. As we can see from Fig. 4, the parasitic resistance of L_s, C_s, and the diodes are in series with R_L when the circuit is in continuous mode (state 1 and state 2). Thus, the parasitic resistance should be far less than R_L to guarantee the power transfer efficiency. Although a small value of R_L can influence the modeling accuracy of the system, such circumstances should be avoided in the first place considering the power losses of the parasitic resistance.

V. Design of the Compensation Network in Primary Side

According to (1), the key to design parameters of *LCC* network in the primary side is to solve X_p and α. As is mentioned above, X_p is the impedance of the three arms of *LCC* network, and α is a factor used to realize ZVS. By changing α, the equivalent output impedance of the inverter is tuned, changing the turn-OFF current (I_{OFF}) of the MOSFETs without effect on the constant-current characteristics of *LCC* network. The minimum turn-OFF current to maintain ZVS can be calculated by [25]

$$I_{\text{off\_min}} = -\frac{2U_d C_{\text{oss}}}{t_d} \tag{50}$$

where C_{oss} is the drain-source junction capacitance of the MOSFETs and t_d is the dead time of the inverter.

The parameters of *LCC* network will be designed with FHA and TD method separately below.

A. FHA Method

1) X_p: With FHA method, X_p can be easily determined by the nominal output power P_{o_n} and nominal load R_{LN}

$$X_p = \frac{\omega M U_d}{\sqrt{P_{o\_n} R_{\text{LN}}}}. \tag{51}$$

2) α: The turn-OFF current can be calculated at time 0, which is

$$I_{\text{inv\_1}}(0) = \frac{4U_d}{\pi X_p^2}[X_f + (\alpha - 1)X_p]. \tag{52}$$

Considering that the equivalent impedance of the secondary side is resistant, it can be deduced that $X_f = 0$; besides, the turn-OFF current should be equal to $I_{\text{OFF\_min}}$ because that a larger value will lead to more conduction losses of the MOSFETs. Therefore,

$$\alpha = 1 + \frac{\pi X_p I_{\text{off\_min}}}{4U_d}. \tag{53}$$

B. TD Method

1) X_p: With TD method, the design of X_p should follow the steps as follows:

Step 1: Calculate U_{RL} with

$$U_{\text{RL}} = \sqrt{P_{o\_n} R_{\text{LN}}}. \tag{54}$$

Step 2: Calculate β with (34) and determine the operating mode of the rectifier with (44): if $\beta < \pi/2$, the rectifier is in CCM; if $\beta \geq \pi/2$, the rectifier is in DCM.

Step 3: Calculate U_s with

$$U_s = G(U_{\text{RL}} + 2V_{d\_f}). \tag{55}$$

The derivation of G depends on the operating mode of the rectifier: if the rectifier is in CCM, $G = \pi/4$; if the rectifier is in DCM, G can be determined by solving (40) and (43) with mathematical calculation tools.

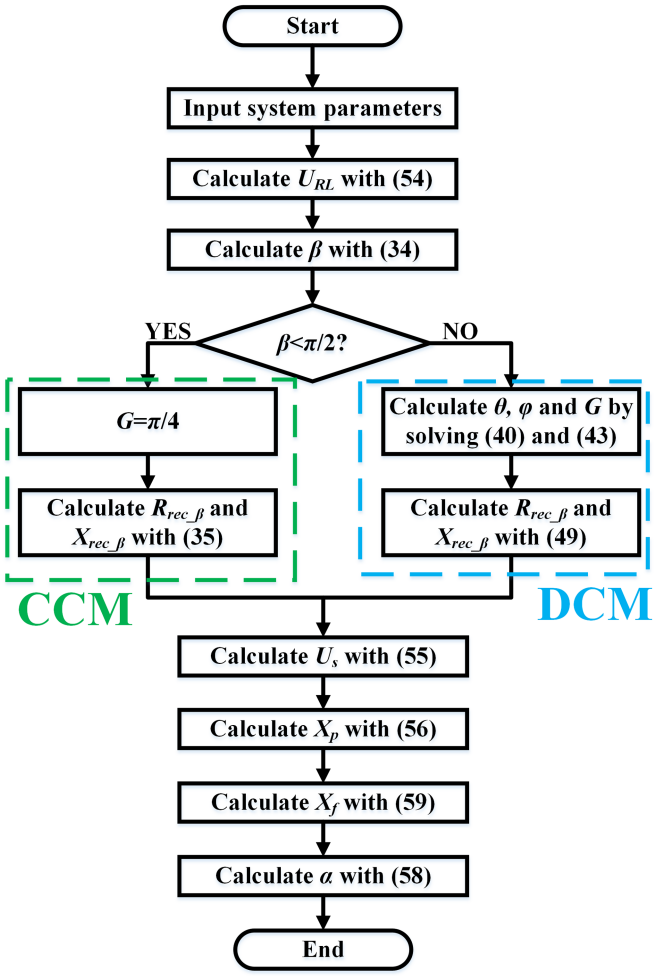

Fig. 9. Flowchart of the designing process for X_p and α with TD method.

Step 4: Calculate X_p by combining (2) and (5), i.e.,

$$X_p = \frac{4\omega M U_d}{\pi U_s}. \tag{56}$$

2) α: According to (13), the turn-OFF current can be derived as

$$i_{\text{inv}(0)} = \frac{4U_d}{\pi X_p}\left(\frac{X_f}{X_p} + \alpha - \frac{5}{4}\right). \tag{57}$$

Thus, α can be calculated as

$$\alpha = \frac{\pi X_p I_{\text{off\_min}}}{4U_d} + \frac{5}{4} - \frac{X_f}{X_p}. \tag{58}$$

As for X_f, it can be derived by

$$X_f = \text{Im}\left\{\frac{\omega^2 M^2}{R_{\text{LS}} + \omega L_s\left(R_{\text{rec}\_\beta} + jX_{\text{rec}\_\beta}\right)}\right\} \tag{59}$$

where R_{rec_β} and X_{rec_β} can be calculated with (35) or (49), depending on the operating mode of the rectifier.

A flowchart of the designing process is showing in Fig. 9.

VI. Estimation of the Load

To estimate the load of WPT system from the primary side, the reflected impedance Z_f is needed to be known. The voltage and current of the primary-side coil is measured in literature to calculate Z_f, which takes high sampling rates considering the high frequency of the power transfer. In this article, instead, Z_f is calculated in a simpler way.

As shown in (17), the output current of inverter i_{inv} is related with R_f, X_f, and time t. At time 0, i_{inv} is the turn-OFF current of the MOSFETs, which is shown in (57); at time $\pi/2\omega$ (quarter of the cycle), i_{inv} can be derived as

$$i_{\text{inv}}\left(\frac{\pi}{2\omega}\right)=\frac{4U_dR_f}{\pi X_p^2}. \tag{60}$$

To measure $i_{\text{inv}}(0)$ and $i_{\text{inv}}(\pi/2\omega)$, the output voltage u_{inv} should also be measured as a reference. The detailed process is as follows:

1) The rising edge of u_{inv} is detected, the time is recorded as t_0, and the current through L_f at t_0 is sampled as $i_{\text{inv}}(0)$.
2) Time is counted from t_0 to $\pi/2\omega$, and the current through L_f at time $\pi/2\omega$ is sampled as $i_{\text{inv}}(\pi/2\omega)$.

With this method, the sampling rate is much more reduced, and the complexity of calculation is also lowered.

Assume that

$$\lambda=\frac{\pi X_p^2}{4U_d}. \tag{61}$$

It can be derived that

$$\begin{cases}R_f=\lambda i_{\text{inv}}(\frac{\pi}{2\omega})\\ X_f=\lambda i_{\text{inv}}(0)+(\frac{5}{4}-\alpha)X_p.\end{cases} \tag{62}$$

Once Z_f is known, the input impedance of the rectifier, Z_{rec} can be calculated by

$$Z_{\text{rec}}=\frac{\omega^2M^2}{R_f-R_{\text{LP}}+jX_f}-R_{\text{LS}}. \tag{63}$$

According to (35) and (49), $R_{\text{rec\_}\beta}$ and $X_{\text{rec\_}\beta}$ are only related to β (whether in CCM or DCM), and it can be seen in Fig. 8 that the $R_{\text{rec\_}\beta}-\beta$ and $X_{\text{rec\_}\beta}-\beta$ curves are both monotonous and can be used to estimate R_L. To facilitate the estimation, the curves in Fig. 8 are approximated with curve fitting method (as shown in Fig. 10) and we choose $R_{\text{rec\_}\beta}$ to estimate R_L. After curve fitting, the relation of $R_{\text{rec\_}\beta}-\beta$ can be approximated as

$$\begin{aligned}\beta\approx&-0.0008722R_{\text{rec\_}\beta}^5+0.01633R_{rec\_\beta}^4-0.1187R_{rec\_\beta}^3\\&+0.4305R_{rec\_\beta}^2+0.9803R_{rec\_\beta}+0.02998.\end{aligned} \tag{64}$$

In this article, the mutual inductance of the coupling coils M is measured before the estimation as a preknown parameter. In practice, the coupling coils can be misaligned and the mutual inductance will change, which will influence the accuracy of the estimation. In the previous articles, there are estimation of both mutual inductance and load [31], [34]. However, if the load varies in a large range, the estimation may face the two-solution problem [33], [34]. Therefore, the proposed load estimation method can be deemed as a phasic study and we will try to solve the two-solution problem in the future article to estimate both the mutual inductance and load.

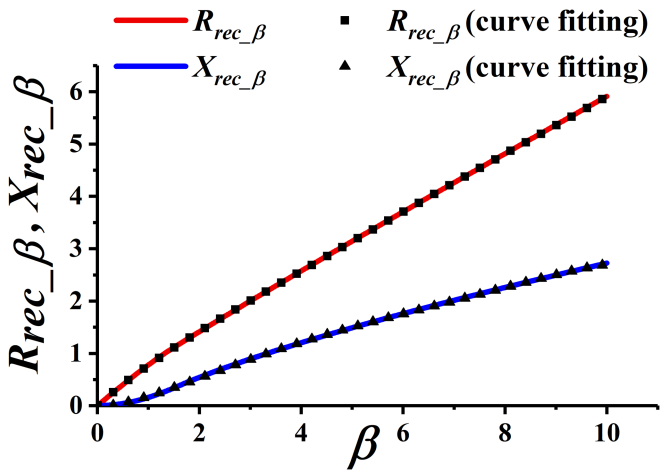

Fig. 10. Curving fitting of $R_{\text{rec\_}\beta}-\beta$ and $X_{\text{rec\_}\beta}-\beta$.

TABLE I
Parameters of the System

Parameter	Value
f/kHz	50
U_d/V	200
C_d/μF	150
C_L/μF	200
R_L/ohm	10–200
L_p/μH	238.18
L_s/μH	129.46
M/μH	52.89 (align)
P_{o_n}/W	1000
$I_{\text{off\_min}}$/A	–2.5

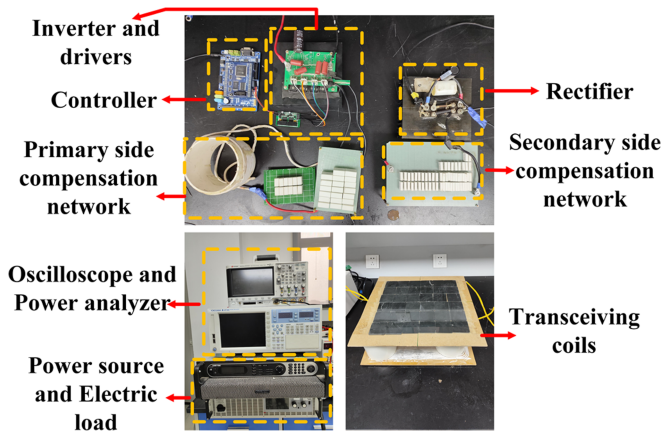

Fig. 11. Built experimental prototype.

VII. Simulation and Experimental Verification

To verify the proposed analysis, design, and load estimation method, simulation and experiments are conducted based on parameters in Table I. An experimental prototype is built as shown in Fig. 11, the primary-side coil is 20-turn with the size of 35 cm × 35 cm and the secondary-side coil is 13-turn with the

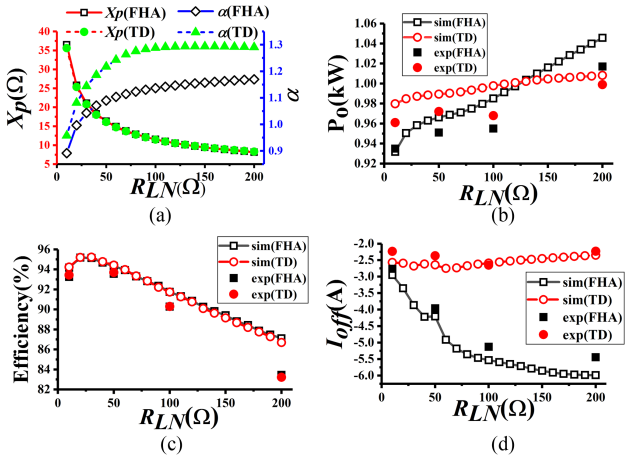

Fig. 12. Results of parameter design, simulation, and experiments. (a) Designed X_p and α. (b) Output power. (c) Power transfer efficiency. (d) Turn-OFF current.

size of 30 cm × 30 cm. Four IPW65R080 MOSFETs are used in the inverter and two IXYS DSEI 2X101 diode modules comprise the rectifier, a TI DSP TMS320F28335 is used as the controller.

A. Parameter Design

The parameters of *LCC* network in the primary side are designed based on nominal load (R_{LN}) of 10–200 Ω with FHA and TD method, as shown in Fig. 12(a). As the figure shows, the values of X_p designed by FHA and TD method are very close, while the values of α are significantly different.

Fig. 12(b)–(d) shows the output power, efficiency, and turn-OFF current of the WPT system in the simulation and experiments, where the value of load 10, 50, 100, and 200 Ω were chosen to simplify the verification. The output power [Fig. 12(b)] of WPT system designed by TD method is more stable compared with that designed by FHA method, which reflects the difference of modeling accuracy between the two methods. Noted that the output power deviates from the nominal power, no matter for FHA method or TD method. The main reason is the ignorance of the parasitic resistance of components in modeling and designing of the system. The output power seems to rise with the increase of nominal load because the current flowing through the electronic components in large-nominal-load system is smaller than that in the smaller-nominal-load system, leading to less power losses. The transfer efficiency [Fig. 12(c)] curves of the two methods are very close, no matter in simulation or experiments. The turn-OFF current [Fig. 12(d)], determined by α, are quite different: for TD method, it can be close to the target value (−2.5 A); for FHA method, it can deviate from the target value with the increase of load. Although the turn-OFF current of FHA method also meets the need of ZVS, its large value for light load can cause more switching losses.

B. Verification of the TD Modeling

Fig. 13 shows the waveforms of the output voltage, current of the inverter (U_{inv}, I_{inv}) and the input voltage, and current of

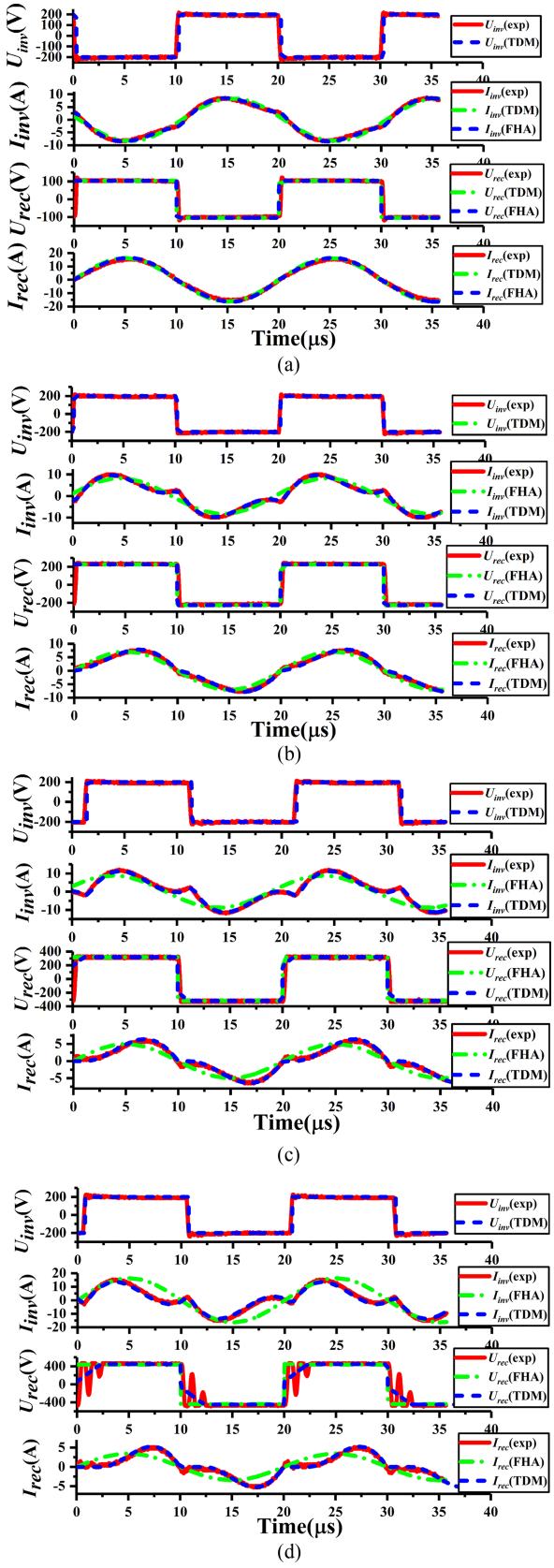

Fig. 13. Waveforms of U_{inv}, I_{inv}, U_{rec}, and I_{rec}. (a) $R_{LN} = 10\ \Omega$. (b) $R_{LN} = 50\ \Omega$. (c) $R_{LN} = 100\ \Omega$. (d) $R_{LN} = 200\ \Omega$.

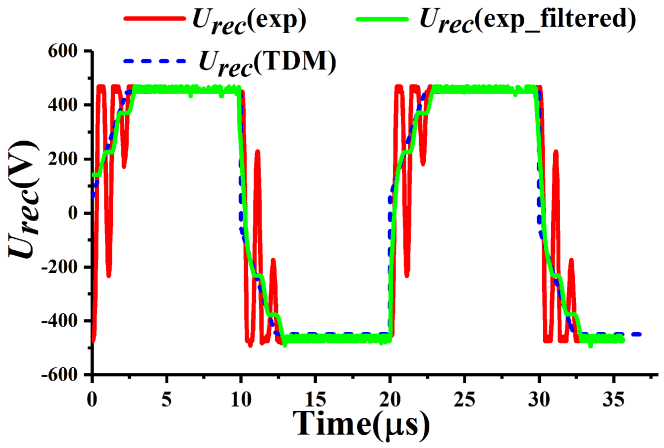

Fig. 14. Filtered waveform of $U_{\rm rec}$ ($R_{\rm LN} = 200\ \Omega$).

the rectifier ($U_{\rm rec}$, $I_{\rm rec}$) in CCM and DCM. To verify the accuracy of TDA, the waveforms based on FHA and time-domain modeling (TDM) are also depicted in the figure. When $R_{\rm LN} = 10\ \Omega$ [Fig. 13(a)], the rectifier is in CCM, both FHA and TDM feature the experimental results very well. When $R_{\rm LN} = 50\ \Omega$ [Fig. 13(b)], the rectifier is still in CCM, the TDM shows high accuracy, while slight errors occur with FHA. When $R_{\rm LN} = 100\ \Omega$ [Fig. 13(c)], the rectifier is in DCM, the TDM also features the experimental results well, while obvious errors occur with FHA. When $R_{\rm LN} = 200\ \Omega$ [Fig. 13(d)], the rectifier is in DCM, there is a resonant superimposed on the waveform of $U_{\rm rec}$, this is because a resonance takes place between L_s and the combination of C_s and the parasitic capacitance of the diodes [24]. Although the TDM does not depict such phenomenon, it shows much higher accuracy than the FHA in depicting $I_{\rm inv}$ and $I_{\rm rec}$. Besides, the mismatch between TDM and the experimental results will not affect the accuracy of the parameter designing, because the process hardly transfers active power to the load, but to the parasitic resistance of L_s, C_s, and the diodes instead. This conclusion can be verified by 1) the output power for $R_{\rm LN} = 200\ \Omega$ in Fig. 12(b) is close to the nominal power (1000 W); and 2) the waveform of $I_{\rm inv}$ in Fig. 13(d) is very close to the experimental one, proving the high accuracy of the modeling in the primary side, which is based on the TDM of the secondary side.

The experimental waveform of $U_{\rm rec}$ is processed with average filter, as shown in Fig. 14. The filtered waveform is close to the theoretical one. In conclusion, the TDM features the experimental results very well.

C. Load Estimation

To verify the proposed load estimation method, experiments are conducted both in state of heavy ($R_{\rm LN} = 50\ \Omega$) and light ($R_{\rm LN} = 100\ \Omega$) nominal load, and the results of load estimation with TD method are compared with the FHA method. It should be noted that the load estimation with FHA method is same with TD method when calculating Z_f, but different in the estimation of $Z_{\rm rec}$; the intention for the former is to simplify the experiments,

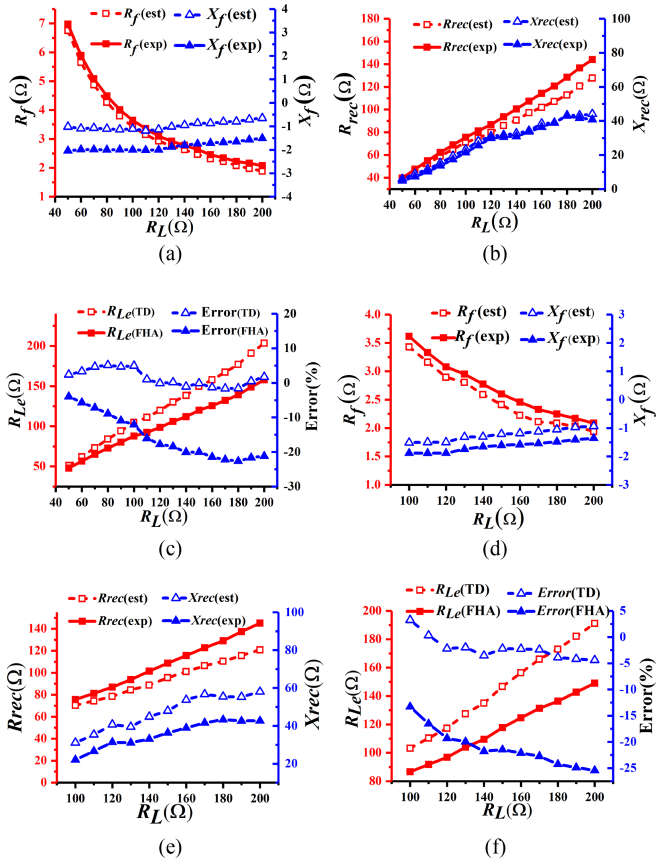

Fig. 15. Results of load estimation. (a) Z_f ($R_{\rm LN} = 50\ \Omega$). (b) Z_{rec} ($R_{\rm LN} = 50\ \Omega$). (c) R_{Le} ($R_{\rm LN} = 50\ \Omega$). (d) Z_f ($R_{\rm LN} = 100\ \Omega$). (e) Z_{rec} ($R_{\rm LN} = 100\ \Omega$). (f) R_{Le} ($R_{\rm LN} = 100\ \Omega$).

and the reason for the latter is a resistive $Z_{\rm rec}$ with FHA method will make much difference compared with TD method.

1) Heavy Nominal Load ($R_{LN} = 50\ \Omega$): The load of the system varies from 50 Ω (heavier load will lead to higher power which will exceed the designed capacity) to 200 Ω and will be estimated with TD and FHA method, respectively. In Fig. 15(a) and (b), the estimated Z_f and $Z_{\rm rec}$ calculated with TD method are compared with the experimental value. It can be seen that the amplitude of $Z_{\rm rec}$ is in reverse ratio with Z_f, and the estimation errors will be superposed with the process of calculation. The estimation of R_L both in TD and FHA method are compared in Fig. 15(c), both the estimated loads are smaller than the real value, while the accuracy of TD method is within 5%, which is better than the FHA method in the whole range of load.

2) Light Nominal Load ($R_{LN} = 100\ \Omega$): The load of the system varies from 100 to 200 Ω and will be estimated with TD and FHA method, respectively. In Fig. 15(d) and (e), the estimated Z_f and $Z_{\rm rec}$ calculated with TD method are compared with the experimental value. Similar with what happened when the nominal load is 50 Ω, the estimation errors will be superposed with the process of calculation. The estimation of R_L both in TD and FHA method are compared in Fig. 15(f), the accuracy of TD method is within 5%, which is much better than the FHA

TABLE II
COMPARISON OF LOAD ESTIMATION METHODS

Literature	Compensation network	Primary-side modeling	Secondary-side modeling	Rectifier mode	Complexity of sampling	Accuracy of estimation
[36]	SS	FHA	FHA	CCM	High	<2%
[37]	*LCC–LCC*	FHA	FHA	——	High	——
[31]	SS	FHA	FHA	——	High	<5%
[29]	*LCC–LCC*	FHA	TD	CCM	High	<8.2%
[33]	*LCC–LCC*	FHA	TD	CCM	Low	<7.9%
[34]	*LCC–LCC*	FHA	TD	CCM and DCM	High	<9%
Proposed	*LCC*–S	Consider harmonics	TD	CCM and DCM	Medium	<5%

method in the whole range of load. The load estimation method is compared with the other method proposed in the literature, as shown in Table II. Among the listed methods, the proposed one in this article takes harmonics in the primary and secondary side in consideration, estimating the load in a wide range with a low-complexity sampling method to achieve a relatively high estimating accuracy.

VIII. CONCLUSION

Based on *LCC*-S compensation network, the WPT system is accurately modeled in this article to design the parameters in the network, and the load is estimated with a simple sampling method. The harmonics in the output current of the inverter is calculated, and the state-space equation in time domain of the rectifier both in CCM and DCM are analyzed, proving that the equivalent input impedance of the rectifier is inductive, which is more accurate than the FHA-based resistive model, especially in DCM. Based on the proposed model, the parameters of the *LCC* network are designed. Compared with the FHA-based designing method, the improvement of the proposed method is mainly the accurate tuning of turn-OFF current of the MOSFETs in the inverter. To estimate the load of the system, the output current of the inverter at time of zero and quarter-cycle from the rising edge of zero crossing point of the output voltage are sampled to calculate the reflected impedance. The proposed method reduces the sampling rate and lowers the complexity of calculation, estimating the load in a wide range within error of 5%. Although the characteristics of the harmonics can also be depicted with simulation tools, a main contribution of this article is to reveal the inherent operation principles of the system, such as the mathematical expressions of the output current of the inverter and input current of the rectifier, the critical condition of CCM and DCM of the rectifier, and the relation of Z_f with the output current of the inverter. All the principles above can facilitate the analysis, design, and parameter estimation of the system, which cannot be derived directly by the simulation.

APPENDIX

A. Discussion About DCM of the Rectifier

When the load is large enough, the rectifier cannot retain CCM, the reason can be explained with proof by contradiction as follows.

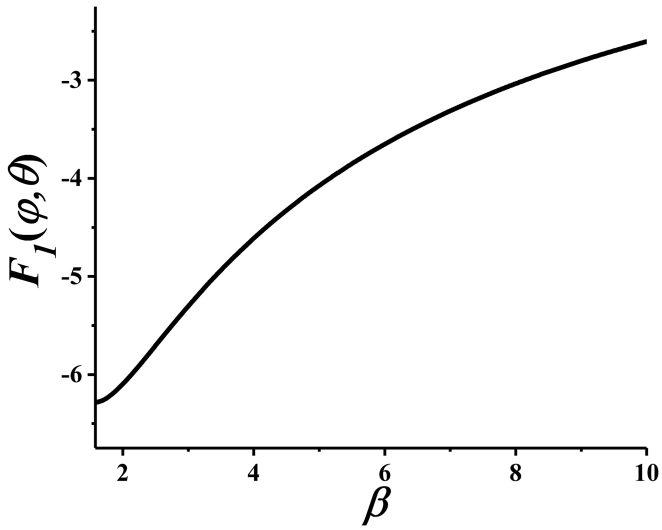

Fig. 16. Relation of $F_1(\varphi,\theta)$ and β.

Assuming that the rectifier operates in CCM when β is higher than $\pi/2$, the current in L_s at time t_{0+} (a positive value infinitely approaching to 0) can be derived according to (25)

$$i_L(t_{0+}) = \frac{U_s \sin(\omega t_{0+})}{\omega L_s}\left(\frac{1}{2}\omega t_{0+} - \frac{\pi}{4} + \frac{\pi^2}{8\beta}\right). \quad \text{(A1)}$$

Considering that $\sin(\omega t_{0+}) > 0$ and ωt_{0+} are infinitely approaching to 0, the sign of $i_L(t_{0+})$ determines on the sign of $(-\pi/4 + \pi^2/8/\beta)$. Therefore, when $\beta > \pi/2$, the sign of $i_L(t_{0+})$ will be negative, which conflicts with Fig. 5. In fact, when $\beta > \pi/2$, $i_L(t)$ will be zero until $u_s(t)$ is large enough to conduct the diodes in the rectifier. In other words, the rectifier will operate in DCM when β is higher than $\pi/2$.

B. Sign of a_u and a_i in DCM of the Rectifier

The value of a_u and a_i in DCM of the rectifier is shown in (46), and the sign of them will be discussed separately as follows.

1) Sign of a_u: From Fig. 7, it can be concluded that the value range of θ in DCM is $-\pi < \theta < 0$; hence, we have $\sin\theta < 0$. Therefore, the sign of a_u is negative.

2) Sign of a_i: According to (40) and (43), $F_1(\varphi,\theta)$ can be calculated with β, as shown in Fig. 16, based on which it can be derived that $F_1(\varphi,\theta) < 0$. The sign of a_i is determined by $F_1(\varphi,\theta)$ and it is also negative.

REFERENCES

[1] G. A. Covic and J. T. Boys, "Inductive power transfer," *Proc. IEEE*, vol. 101, no. 6, pp. 1276–1289, Jun. 2013.

[2] Z. Zhang, H. Pang, A. Georgiadis, and C. Cecati, "Wireless power transfer—An overview," *IEEE Trans. Ind. Electron.*, vol. 66, no. 2, pp. 1044–1058, Feb. 2019.

[3] K. Onai and J. O. Ojo, "Performance analysis and design of frequency controlled series-series compensated inductive power transfer system for electric vehicle battery charging," *IEEE Trans. Ind. Appl.*, vol. 58, no. 1, pp. 962–973, Jan./Feb. 2022.

[4] S. Li, Z. Liu, H. Zhao, L. Zhu, C. Shuai, and Z. Chen, "Wireless power transfer by electric field resonance and its application in dynamic charging," *IEEE Trans. Ind. Electron.*, vol. 63, no. 10, pp. 6602–6612, Oct. 2016.

[5] N. Shinohara, "History and innovation of wireless power transfer via microwaves," *IEEE J. Microw.*, vol. 1, no. 1, pp. 218–228, Jan. 2021.

[6] P. Machura and Q. Li, "A critical review on wireless charging for electric vehicles," *Renewable Sustain. Energy Rev.*, vol. 104, pp. 209–234, 2019.

[7] P. K. Chittoor, B. Chokkalingam, and L. Mihet-Popa, "A review on UAV wireless charging: Fundamentals, applications, charging techniques and standards," *IEEE Access*, vol. 9, pp. 69235–69266, 2021.

[8] I. A. Mashhadi, M. Pahlevani, S. Hor, H. Pahlevani, and E. Adib, "A new wireless power-transfer circuit for retinal prosthesis," *IEEE Trans. Power Electron.*, vol. 34, no. 7, pp. 6425–6439, Jul. 2019.

[9] M. Ursino et al., "Hybrid planar litz coil optimization for phone wireless power transfer," in *Proc. IEEE Appl. Power Electron. Conf. Expo.*, 2021, pp. 1560–1564.

[10] M. Passafiume, G. Collodi, and A. Cidronali, "Improving wireless power transfer efficiency with DC/DC boost charger by multi-sine excitation at 5.8 GHz," *IEEE Microw. Wireless Compon. Lett.*, vol. 32, no. 6, pp. 760–763, Jun. 2022.

[11] Y. Li, J. Zhao, Q. Yang, L. Liu, J. Ma, and X. Zhang, "A novel coil with high misalignment tolerance for wireless power transfer," *IEEE Trans. Magn.*, vol. 55, no. 6, Jun. 2019, Art. no. 2800904.

[12] B. Vardani and N. R. Tummuru, "A single-stage bidirectional inductive power transfer system with closed-loop current control strategy," *IEEE Trans. Transp. Electrific.*, vol. 6, no. 3, pp. 948–957, Mar. 2020.

[13] J. Liu, Z. Liu, and H. Su, "Passivity-based PI control for receiver side of dynamic wireless charging system in electric vehicles," *IEEE Trans. Ind. Electron.*, vol. 69, no. 1, pp. 783–794, Jan. 2022.

[14] A. C. Bagchi, A. Kamineni, R. A. Zane, and R. Carlson, "Review and comparative analysis of topologies and control methods in dynamic wireless charging of electric vehicles," *IEEE J. Emerg. Sel. Topics Power Electron.*, vol. 9, no. 4, pp. 4947–4962, Apr. 2021.

[15] X. Wang et al., "Synthesis and analysis of primary high-order compensation topologies for wireless charging system applying sub-harmonic control," *IEEE Trans. Power Electron.*, vol. 38, no. 7, pp. 9173–9182, Jul. 2023.

[16] W. Zhong, F. Xiang, and C. Hu, "Metal object detection with detection coils perpendicular to power coils for wireless power transfer systems," *IEEE Trans. Power Electron.*, early access, doi: 10.1109/TPEL.2023.3257019.

[17] M. Kiani and M. Ghovanloo, "The circuit theory behind coupled-mode magnetic resonance-based wireless power transmission," *IEEE Trans. Circuits Syst. I: Regular Papers*, vol. 59, no. 9, pp. 2065–2074, Sep. 2012.

[18] T. Imura and Y. Hori, "Maximizing air gap and efficiency of magnetic resonant coupling for wireless power transfer using equivalent circuit and Neumann formula," *IEEE Trans. Ind. Electron.*, vol. 58, no. 10, pp. 4746–4752, Oct. 2011.

[19] S. Boyune et al., "Design of a high power transfer pickup for on-line electric vehicle (OLEV)," in *Proc. IEEE Int. Elect. Veh. Conf.*, 2012, pp. 1–4.

[20] J. Hou, Q. Chen, Z. Zhang, S. C. Wong, and C. K. Tse, "Analysis of output current characteristics for higher order primary compensation in inductive power transfer systems," *IEEE Trans. Power Electron.*, vol. 33, no. 8, pp. 6807–6821, Aug. 2018.

[21] R. Mai, B. Yang, Y. Chen, N. Yang, Z. He, and S. Gao, "A misalignment tolerant ipt system with intermediate coils for constant-current output," *IEEE Trans. Power Electron.*, vol. 34, no. 8, pp. 7151–7155, Aug. 2019.

[22] W. Xiong, Q. Yu, Z. Liu, L. Zhao, Q. Zhu, and M. Su, "A detuning-repeater-based dynamic wireless charging system with quasi-constant output power and reduced inverter count," *IEEE Trans. Power Electron.*, vol. 38, no. 1, pp. 1336–1347, Jan. 2023.

[23] J. Jiang, K. Song, Z. Li, C. Zhu, and Q. Zhang, "System modeling and switching control strategy of wireless power transfer system," *IEEE J. Emerg. Sel. Topics Power Electron.*, vol. 6, no. 3, pp. 1295–1305, Mar. 2018.

[24] A. Safaee and K. Woronowicz, "Time-domain analysis of voltage-driven series–series compensated inductive power transfer topology," *IEEE Trans. Power Electron.*, vol. 32, no. 7, pp. 4981–5003, Jul. 2017.

[25] W. Li, H. Zhao, S. Li, J. Deng, T. Kan, and C. C. Mi, "Integrated *LCC* compensation topology for wireless charger in electric and plug-in electric vehicles," *IEEE Trans. Ind. Electron.*, vol. 62, no. 7, pp. 4215–4225, Jul. 2015.

[26] X. Zhu et al., "High-efficiency WPT system for CC/CV charging based on double-half-bridge inverter topology with variable inductors," *IEEE Trans. Power Electron.*, vol. 37, no. 2, pp. 2437–2448, Feb. 2022.

[27] F. Xu, S. C. Wong, and C. K. Tse, "Overall loss compensation and optimization control in single-stage inductive power transfer converter delivering constant power," *IEEE Trans. Power Electron.*, vol. 37, no. 1, pp. 1146–1158, Jan. 2022.

[28] C. Ma, X. Qu, Y. Li, and J. Liu, "Single-stage active rectifier with wide impedance conversion ratio range for inductive power transfer system delivering constant power," *IEEE Trans. Power Electron.*, vol. 38, no. 6, pp. 7877–7890, Jun. 2023.

[29] Y. Guo, L. Wang, Y. Zhang, S. Li, and C. Liao, "Rectifier load analysis for electric vehicle wireless charging system," *IEEE Trans. Ind. Electron.*, vol. 65, no. 9, pp. 6970–6982, Sep. 2018.

[30] Y. Guo, Y. Zhang, Q. Bo, Z. Liu, J. Meng, and L. Wang, "Approximate linearization of rectifier load in wireless power transfer systems," in *Proc. IEEE PELS Workshop Emerg. Technol., Wireless Power Transfer*, 2020, pp. 74–78.

[31] R. Dai, W. Zhou, Y. Chen, Z. Zhu, and R. Mai, "Pulse density modulation based mutual inductance and load resistance identification method for wireless power transfer system," *IEEE Trans. Power Electron.*, vol. 37, no. 8, pp. 9933–9943, Aug. 2022.

[32] Z. H. Wang, Y. P. Li, Y. Sun, C. S. Tang, and X. Lv, "Load detection model of voltage-fed inductive power transfer system," *IEEE Trans. Power Electron.*, vol. 28, no. 11, pp. 5233–5243, Nov. 2013.

[33] Y. Guo, Y. Zhang, S. Li, C. Tao, and L. Wang, "Load parameter joint identification of wireless power transfer system based on the dc input current and phase-shift angle," *IEEE Trans. Power Electron.*, vol. 35, no. 10, pp. 10542–10553, Oct. 2020.

[34] S. Li, L. Wang, Y. Guo, and Z. Liu, "Flexible energy-transfer control of dynamic wireless power transfer system based on estimation of load and mutual inductance," *IEEE Trans. Ind. Appl.*, vol. 58, no. 1, pp. 1157–1167, Jan. 2022.

[35] S. Li, W. Li, J. Deng, T. D. Nguyen, and C. C. Mi, "A double-sided LCC compensation network and its tuning method for wireless power transfer," *IEEE Trans. Veh. Technol.*, vol. 64, no. 6, pp. 2261–2273, Jun. 2015.

[36] Y. Yang, Y. Jiang, S. C. Tan, and S. Y. R. Hui, "A frequency-sweep based load monitoring method for weakly-coupled series-series compensated wireless power transfer systems," in *Proc. IEEE PELS Workshop Emerg. Technol.: Wireless Power Transfer*, 2018, pp. 1–5.

[37] Q. Zhao, A. Wang, J. Liu, and X. Wang, "The load estimation and power tracking integrated control strategy for dual-sides controlled LCC compensated wireless charging system," *IEEE Access*, vol. 7, pp. 75749–75761, 2019.

Shufan Li received the Ph.D. degree in electrical engineering from the Institute of Electrical Engineering, Chinese Academy of Sciences, Beijing, China, in 2020.

He is currently an Associate Professor with the Department of Vehicle Energy System and Control Technology, Institute of Electrical Engineering, Chinese Academy of Sciences. His research interests include analysis, designing, and controlling of static/dynamic wireless power transfer system.

Fang Li received the Ph.D. degree in electrical engineering from the Institute of Electrical Engineering, Chinese Academy of Sciences, Beijing, China, in 2009.

She is currently an Associate Professor with the Department of Vehicle Energy System and Control Technology, Institute of Electrical Engineering. Her research interests include wireless power transmission, simultaneous wireless information and power transfer, and intelligent vehicle control.

Rong Zhang received the M.S. degree in electrical engineering from the North China University of Technology, Beijing, China, in 2019.

He is currently an Associate Professor with the Department of Vehicle Energy System and Control Technology, Institute of Electrical Engineering, Chinese Academy of Sciences. His research interests include designing and control of power converters, and optical communication technology.

Chengxuan Tao (Member, IEEE) received the M.S. degree in control science and engineering from the Chongqing University, Chongqing, China, in 2012. He is currently working toward the Ph.D. degree in mechanical engineering with the Beijing Institute of Technology, Beijing, China.

He is currently a Senior Engineer with the Key Laboratory of Power Electronics and Electric Drives, Chinese Academy of Sciences, Beijing, China. His research interests include circuit topology, analysis and control of wireless power transfer system, especially its applications in special fields.

Lifang Wang (Member, IEEE) received the Ph.D. degree in automotive engineering from the Jilin University, Jilin, China, in 1997.

She joined the Institute of Electrical Engineering, Chinese Academy of Sciences (IEECAS), Beijing, China. During the Chinese tenth-five-year plan (2001–2005), she was a member of the national specialist group of Key Special Electric Vehicle Project of the National 863 Program, and she was the Head of the 863 Special EV Project Office. She is currently the Director of the Department of Vehicle Energy System and Control Technology, IEECAS. She is also the Vice Director of the Key Laboratory of Power Electronics and Electric Drives, Chinese Academy of Sciences. Her research interests include wireless charging system for EV, EV control system, EV battery management system, electromagnetic compatibility, and smart electricity use.